RSC Advances

PAPER

View Article Online
View Journal | View Issue



Cite this: *RSC Adv.*, 2014, **4**, 8157

# Nonadiabatic structure instability of planar hexagonal gold cluster cation $Au_7$ and its spectral signature

J. R. Soto,*[a] B. Molina[a] and J. J. Castro[b]

Received 7th November 2013
Accepted 14th January 2014

DOI: 10.1039/c3ra46463f

www.rsc.org/advances

Determining the structure for gold nanoclusters at which the 2D–3D transition occurs has been a challenging problem for both theoretical and experimental studies. For gold cation clusters, quantum chemistry calculations have produced controversial results concerning the last most stable planar structure, some indicating that corresponds to $n = 7$, whereas others conclude that at this value, the structure is already 3D. Experimentally, ion mobility spectroscopy measurements, assisted by DFT calculations, have been interpreted as a planar structure for $Au_7^+$. Here, we show that the usually assumed 2D non-degenerate ground state cluster structure for $Au_7^+$ with $D_{6h}$ symmetry is unstable against a puckering distortion, ending in a 3D stable structure with $D_{3d}$ symmetry. The analysis is based on the pseudo Jahn–Teller effect through vibronic coupling between the ground state and two excited states. This structure presents, in average, the same surface area than the 2D, being therefore compatible with experimental results. We discuss the effects the vibronic coupling would have on Raman, IR and UV-vis spectra. The study is based on a scalar and spin orbit relativistic DFT calculation in the Zero Order Regular Approximation (ZORA).

## 1 Introduction

The fact that small clusters and nanostructures present a completely different physical and chemical behavior than their constituent atoms and bulk phases, has opened an intense field of research for more than two decades. In particular, the study of gold nanoclusters, both supported and on the gas phase, has been of special interest due to their unique catalytic properties when compared to other metallic clusters.[1,2] One of the main characteristics that has given gold nanoclusters their particular physical–chemical properties is the relevance of relativistic effects in determining their stable structure and electronic configuration.[3–10] It has been suggested that those relativistic effects are responsible for observing planar structures for gold nanoclusters with larger number of atoms than silver and cooper.[11–18] For anionic and neutral clusters, gold planar structures have been reported for a number of atoms as high as 13, whereas for silver and cooper, planar structures correspond to less than 7 atoms. For cations, the highest number of atoms reported are 8 and 5 respectively.[19–21]

Recently, new experimental techniques have been developed to study the geometrical structure of both gaseous and supported gold nanoclusters in different charged states.[22–24] The study of nanoclusters on the gas phase provides a natural framework to understanding the dependence of those properties on the size and structure stability of the small clusters. For gas phase clusters, analysis of anionic structures are mainly based on photoelectron spectroscopy,[25] electron diffraction,[26] and ion mobility spectroscopy,[19] whereas for cations, only the ion mobility technique and photodissociation spectroscopy[27] have proved to be successful. All those experimental methods are not able to determine in a unique way the geometrical structure, therefore they must be complemented with theoretical predictions, being the density functional theory (DFT) the most widely accepted methodology.

From a theoretical point of view, gold clusters are characterized by a rather flat adiabatic potential energy surface (APES) with several minima, differing in energy by no more than 200 meV,[3,23] presenting therefore the difficulty in finding the global minima. The flatness of the APES, together with the dependence of some of the results on the functional and basis used in DFT calculations,[3,4] has made the analysis of the possible lowest-energy structure for a given isomer, a difficult and challenging problem, being the determination of the critical number of atoms for the 2D–3D transition a typical example.[11,13,28–38]

For small cationic gold clusters, DFT theoretical predictions have produced controversial results concerning the 2D–3D transition structure.[14,20,21,39,40] Calculations with B3LYP[41] and PBE[42] exchange correlation functionals and Stuttgart[43] relativistic effective core pseudopotential (RECPs) conclude that the

[a]*Facultad de Ciencias, Universidad Nacional Autónoma de México, Apdo. Post. 70-646, 04510 México D.F., México. E-mail: jrsoto@unam.mx; Fax: +52 55 5616 0326; Tel: +52 55 5622 4871*

[b]*CINVESTAV del IPN, Departamento de Física, Apdo. Post. 14-740, 07000 México D.F, México*

$Au_7^+$ cluster is the last planar structure with $D_{6h}$ symmetry,[40,44] whereas the same functional with LANL2DZ2 (ref. 45) and Ermler[46] pseudopotentials predicts a 3D hexagonal isomer (puckered) with $D_{3d}$ symmetry, with dihedral angles of 31.6° *y* 31.5°.[40] Also, the BP86 (ref. 47 and 48) functional with Ermler pseudpotential predicts a puckered structure with a dihedral angle of 27.5°.[40] Based on these results, Remacle and Kryachko[40] concluded that for cationic gold clusters, the number of gold atoms at which the 2D–3D transition occurs is 7 and not 8. Experimentally, cross-section measurements using ion mobility spectroscopy assisted by DFT calculations (BP86/Sttutgart)[39] support the prediction that $D_{6h}$ $Au_7^+$ is still 2D. Photodissociation spectra experiments, compared with predictions of dipole allowed transitions calculated with time dependent DFT (TDDFT), as applied to cluster structures from DFT (B3LYP) and MP2,[27] were also interpreted as a planar structure for $Au_7^+$, however the authors theoretically found that the planar structure has to be distorted, resembling cyclohexane in chair formation; similar to that reported by Remackle and Kryachko. The controversy between these results and 3D structure with symmetry $D_{3d}$ is reminiscent of the problem of stability in ring planar structures on some cyclic organic compounds. It has been reported in the literature on this subject the presence of instabilities towards out of plane vibrational puckering modes, in either the ground or excited state structures. This kind of instability has been interpreted as originated from a pseudo Jahn–Teller (PJT) effect, resulting from the coupling between that particular state with one or several excited states.[49–51] The PJT effect can also occur in combination with other vibronic couplings.[52]

In this work, inspired by the instability of planar structures on several organic ring structures, we study the 2D–3D transition of the ground state of $Au_7^+$ cluster through a puckered structure arising from a PJT effect. Since the ground state with $D_{6h}$ symmetry, which is among the most stable reported structures, is non-degenerate, the only possible instability might arises from a PJT vibronic coupling.[53,54] We perform PBE (scalar and spin-orbit relativistic) DFT calculations at the zero order regular approximation (ZORA), to show that the $Au_7^+$ cluster with $D_{6h}$ symmetry is unstable due to a vibronic coupling which induce a distortion to a stable 3D structure with symmetry $D_{3d}$. We carry out TDDFT calculations for the $D_{6h}$ structure to study the coupling of the ground state with exited states and propose a model of three states linearly coupled to explain the instability of the ground state. Also, we calculated IR, Raman and UV-vis spectra for $D_{3d}$ and $D_{6h}$ $Au_7^+$ cluster and show the existence of shifts, peaks and transitions that are characteristic of the vibronic coupling, which might be the experimental signature of the puckering effect.

## 2 Computational details

The energy calculations, stability analysis and spectral properties in this work are based on DFT and TDDFT studies, using GGA-PBE functional and all electron QZ4P basis set. As the relativistic approximated Hamiltonian, we consider the scalar zero order regular approximation (ZORA), as implemented in Amsterdam Density Functional (ADF 2012.1)[55] with spin-restricted condition.[56,57] For the purpose of studying the dependance of the structure stability on the functional used, and to compare with predictions found in the literature, we calculate the electronic and structural properties for the $Au_7^+$ cluster in the $D_{6h}$ and $D_{3d}$ symmetries for several functionals/basis sets as are implemented in Gaussian03 (ref. 58) and ADF. In Gaussian03, the exchange and correlation interaction were approximated through the parametrizations BP86 and PBE of the generalized gradient approximation (GGA), and the hybrid B3LYP functional. The relativistic effects were probed independently, for both pseudopotentials, LANL2DZ and Stuttgart, with 19 valence electrons each. The DFT calculations, within ADF, were carried out employing the functionals: PBE (GGA), TPSS[59] (meta-GGA), M06L[60] (meta-GGA), and PBE with restricted spin-orbit ZORA. The calculations for the first two functionals were done with and without dispersion corrected terms.

The geometry optimization was performed using a quasi-Newton method with the BFGS Hessian matrix update formula. The optimization of the different skeletal structures of the $Au_7^+$ cluster was done following the method of Molina *et al.*,[61] by trying all possible distorted Jahn–Teller symmetries as symmetry constrictions. In order to improve the SCF convergence we kept an accuracy of $10^{-6}$ Hartree, and for the optimization a gradient maximum limit of $10^{-5}$ Hartree $Å^{-1}$. The stability of the optimized structures was determined by frequency calculations.

The singlet to singlet electronic transitions for the first thirty excited states were evaluated for the $D_{6h}$ and $D_{3d}$ clusters using the TDDFT with ZORA scalar and QZ4P basis as is implemented in ADF. The simulated UV-vis spectra were evaluated for the first forty optically allowed electronic transitions.

## 3 Results and discussion

### 3.1 PJT coupling in $D_{6h}$ $Au_7^+$ cluster

Table 1, shows a comparative analysis of the electronic and structural properties for the $D_{6h}$ $Au_7^+$ cluster for 12 different

Table 1 Electronic and structural properties for the $D_{6h}$ $Au_7^+$ cluster for different methods[a]

| Functional/basis[b] | $\Delta E_{HL}$ | $d_{Au-Au}$ | $\omega$ |
|---|---|---|---|
| B3LYP/LANL2DZ | 2.92 | 2.79 | 10.9i |
| B3LYP/STUTTGART | 2.94 | 2.78 | 17.2i |
| BP86/LANL2DZ | 1.85 | 2.76 | 12.9i |
| BP86/STUTTGART | 1.84 | 2.76 | 7.7 |
| PBE/LANL2DZ | 1.85 | 2.76 | 14.0i |
| PBE/STUTTGART | 1.85 | 2.76 | 6.9 |
| M06L (SR ZORA)/QZ4P | 2.02 | 2.72 | 13.1i |
| TPSS (SR ZORA)/QZ4P | 1.89 | 2.69 | 11.7i |
| TPSS-D (SR ZORA)/QZ4P | 1.89 | 2.69 | 16.1i |
| PBE(SR ZORA)/QZ4P | 1.80 | 2.71 | 12.4i |
| PBE-D (SR ZORA)/QZ4P | 1.80 | 2.70 | 14.5i |
| PBE(SO ZORA)/QZ4P | 1.35 | 2.69 | 15.6i |

[a] HOMO–LUMO energy gap $\Delta E_{HL}$ (eV), distance Au–Au ($d_{Au-Au}$, Å) and lowest frequency $\omega$ ($cm^{-1}$). [b] Six firsts methods were implemented in Gaussian package; the last six in ADF.

 

functional/basis combinations. There, we present the results of the calculated HOMO–LUMO energy gap, distance between gold atoms, and lowest frequency, resulting from the structure optimization calculations. The comparison is made among the hybrid (B3LYP), GGA (BP86, PBE), meta-GGA (MO6L, TPSS), and dispersion corrected (PBE-D, TPSS-D) functionals, with the last six within the ZORA approximation. It should be notice that the calculated bond lengths, for the first six methods, are in the range between 2.76 and 2.79 Å, whereas the corresponding ZORA calculations, predict shorter Au–Au distances, ranging between 2.69 and 2.72 Å. This might be a result of a better relativistic approximation (ZORA) and a greater basis (all electron QZ4P).

The HOMO–LUMO (HL) gaps obtained for the first six methods are larger than $Au_{20}$ (1.77 eV),[62] being the B3LYP HL gaps considerably overestimated, as it has been reported for other gold clusters.[63] The ZORA-SR HL gaps for all methods, except M06L, are in the range between 1.8 and 1.89 eV, and are in good agreement with the corresponding BP86, PBE/LANL2DZ and PBE/STUTTGART calculations; whereas the ZORA-SO is the smallest, due to the extra splitting of the electronic structure produced by the spin-orbit (SO) effect. As can be seen in Table 1, the inclusion of dispersion corrections shows no effect on the bond length or in the HL gap, for the two tested methods. Apparently, the large HL-gaps obtained for the $D_{6h}$ $Au_7^+$ cluster would be related with its molecular stability; however, as it is shown in Table 1, this structure presents one imaginary frequency for every method, except for the BP86 and PBE both with the STUTTGART pseudopotential, implying a lack of an APES minimum and therefore subject to an instability through a vibronic distortion. This distortion should be in the direction of the Jahn–Teller or pseudo-Jahn–Teller active vibrational modes. Since the calculated total electronic wave function corresponds to a closed shell $a_{1g}$ state, the cation structure is not subject to a Jahn–Teller distortion. However, this does not rule out a possible PJT vibronic coupling, since as it has been shown, this is the only cause of instability of high-symmetry configurations of molecular systems in nondegenerate states.[53] This situation might arises as a result of the presence of non-degenerate electronic states strongly interacting under the nuclear displacements in the direction of instability (Kramers degeneracy being an exception). In the particular case of the isomer $Au_7^+$ with symmetry $D_{6h}$, the instability of its non-degenerate ground state can be explained as the result of a strong coupling between the ground state and one or a few excited states, which could be degenerate or quasi-degenerate with possible interaction among them under nuclear displacements.

The isomer $Au_7^+$ with symmetry $D_{6h}$ possesses 15 vibrational modes, with 10 different frequencies whose representation is given by the decomposition:

$$\Gamma_{vib} = A_{1g} + B_{1g} + 2E_{2g} + A_{2u} + B_{1u} + B_{2u} + 2E_{1u} + E_{2u} \quad (1)$$

of which, the modes ($A_{1g}$ + $2E_{2g}$) are Raman-active, whereas ($A_{2u}$ + $2E_{1u}$) are IR-active and the left four modes ($B_{1g}$ + $B_{1u}$ + $B_{2u}$ + $E_{2u}$) are optically silent, all to first order. This structure can be subject to seven different types of symmetry breaking (four corresponding to non-degenerate and three to degenerate normal modes), going to five possible structures with lower symmetry $D_{3d}$, $C_{6v}$, $C_{2v}$, $D_{2h}$ y $C_2$. We performed structure optimization calculations for each symmetry, obtaining a positive energy gain only for the symmetry reduction $D_{6h}$ to $D_{3d}$ (see Fig. 1), which is mediated by the non-degenerate $B_{1g}$ puckering vibrational mode. This mode moves contiguous gold atoms in opposite normal directions to the hexagonal plane (see Fig. 2). The puckering mode coincides with that which had an imaginary frequency for the $D_{6h}$ isomer, agreeing therefore with the direction of the symmetry transition. Hence, the coupling of the ground state has to be mainly with a non-degenerate excited state with symmetry $b_{1g}$. This is a result of the general condition that the vibrational mode that mediates the coupling $\bar{\Gamma}$, must be included in the direct product of the irreducible representations (irreps) between the ground state $\Gamma$, and the excited state $\Gamma'$.

$$\bar{\Gamma} \in \Gamma \times \Gamma' \quad (2)$$

As shown in Table 1, the bond-length and HL-gap predictions by PBE/ZORA are in good agreement with those corresponding to more sophisticated/expensive meta-GGA methods, such as TPSS. Hence, we consider appropriate to use PBE/ZORA for the TDDFT calculations of the excited states. In order to study the possible PJT couplings, we performed TDDFT calculations for the first thirty excited states for singlet to singlet transitions. The results for the first twenty states are shown in Table 2. It can be seen that the 14$^{th}$ singlet–singlet transition satisfy the condition given by eqn (2), *i.e.*, the coupling between the ground state with the excited state is mediated by a $B_{1g}$ mode, and also that the 14$^{th}$ and 15$^{th}$ singlet–singlet excitations are quasi-degenerate with a $\Delta E$ of the order of 4 meV. Their irreps correspond to $b_{1g}$ and $a_{1g}$ respectively, and can also be coupled to each other by the vibrational mode $B_{1g}$ through a PJT

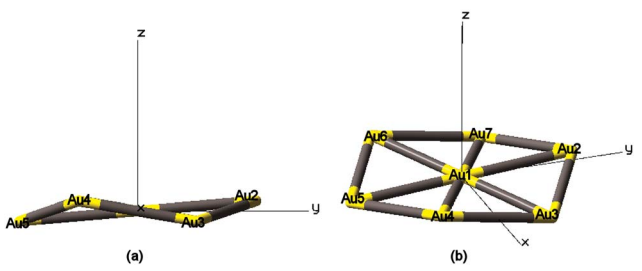


Fig. 1 Minimum energy $D_{3d}$ puckered structure (a) side view, (b) top view.

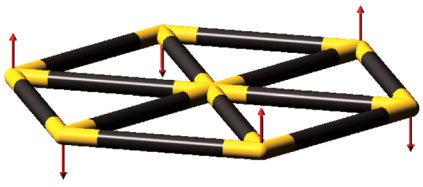

Fig. 2 Schematic diagram of the displacements of the puckering mode in the $D_{6h}$ $Au_7^+$ cluster.

Table 2 Singlet–singlet lowest calculated electronic excitations for the $D_{6h}$ $Au_7^+$ cluster[a]

| Number | $E_{ss}$ | irrep |
|---|---|---|
| 1 | 1.865 | $1b_{2u}$ |
| 2 | 1.984 | $1e_{2g}$ |
| 3 | 1.984 | $1e_{2g}$ |
| 4 | 1.995 | $1a_{2g}$ |
| 5 | 2.025 | $1b_{1u}$ |
| 6 | 2.054 | $1e_{2u}$ |
| 7 | 2.054 | $1e_{2u}$ |
| 8 | 2.057 | $1e_{1u}$ |
| 9 | 2.057 | $1e_{1u}$ |
| 10 | 2.093 | $2e_{2g}$ |
| 11 | 2.093 | $2e_{2g}$ |
| 12 | 2.285 | $2e_{1u}$ |
| 13 | 2.285 | $2e_{1u}$ |
| 14 | 2.335 | $1b_{1g}$ |
| 15 | 2.339 | $1a_{1g}$ |
| 16 | 2.353 | $1e_{1g}$ |
| 17 | 2.353 | $1e_{1g}$ |
| 18 | 2.356 | $1b_{2g}$ |
| 19 | 2.464 | $2a_{2g}$ |
| 20 | 2.504 | $3e_{2g}$ |

[a] $E_{ss}$ are the transition energies (in eV) singlet–singlet.

coupling. These transitions are dominantly between the HOMO-5 ($16e_{1g}$) and HOMO -2 ($29e_{2g}$) to the LUMO ($30e_{2g}$), with weights 0.9814 and 0.9602 respectively. However, to make the ground state unstable, it is necessary to couple it with at least one of those quasi-degenerate excited states mediated by the same vibrational mode. This is a problem of the kind $(1a_{1g} + 2a_{1g} + b_{1g}) \otimes B_{1g}$ where the first state corresponds to the ground state, and the following two to the excited states, being equivalent to two combined PJT couplings. Within the linear coupling model, the APES for the three states, which are the solutions of the vibronic equations are given by[53]

$$\varepsilon_\nu = \frac{1}{2}k_\nu Q^2 + \lambda_\nu(Q),\ \nu = 0, 1, 2 \tag{3}$$

where $k_\nu$ are the non vibronic force constants and $\lambda_\nu(Q)$ are the roots of the secular equation

$$\|W_{\gamma\gamma'} - \lambda_\nu I\| = 0,\ \gamma\gamma' = 0,\ 1,\ 2. \tag{4}$$

If the symmetrized coordinate $Q$ goes along the $B_{1g}$ mode, the $W$ matrix is given by

$$W = \begin{pmatrix} -\Delta_1 & \alpha_{01}Q & 0 \\ \alpha_{01}Q & (\Delta_1 + \Delta_2) & \alpha_{12}Q \\ 0 & \alpha_{12}Q & (\Delta_1 - \Delta_2) \end{pmatrix} \tag{5}$$

were $2\Delta_1$ and $2\Delta_2$ are the energy gaps between the ground state and the $b_{1g}$ excited state and between excited states respectively, and $\alpha_{ij}$ are the linear coupling constants:

$$\alpha_{ij} = \left\langle i \left| \frac{\partial V(Q)}{\partial Q} \right| j \right\rangle \tag{6}$$

being $V$ the electron–nucleon interaction operator.

Eqn (4) is a three-degree polynomial whose solutions, substituted in eqn (3), lead to the PJT APES states. The semi-gaps, $\Delta_1 = 1.167$ and $\Delta_2 = 0.002$ are given from the calculated TDDFT electronic excitations (Table 2); and the PJT parameters are determined by fitting to the corresponding TDDFT APES states calculated for $Q \in$ (0, 0.4 Å], with $\Delta Q = 0.05$ Å. Fig. 3 shows the ground and excited APES states as a function of the symmetrized coordinate $Q$, for the linear PJT model and TDDFT calculations. Fig. 3(a–d) and (a′–d′) correspond to the ground and excited states respectively for four different sets of coupling and force constants. The first three sets were selected to show how the PJT APES depend on the parameters, whereas the last one corresponds to the fitting values. In Fig. 3(a) we set the coupling constant $\alpha_{01} = 0$, *i.e.*, there is no coupling between the ground and $b_{1g}$ excited states; therefore, the ground state has

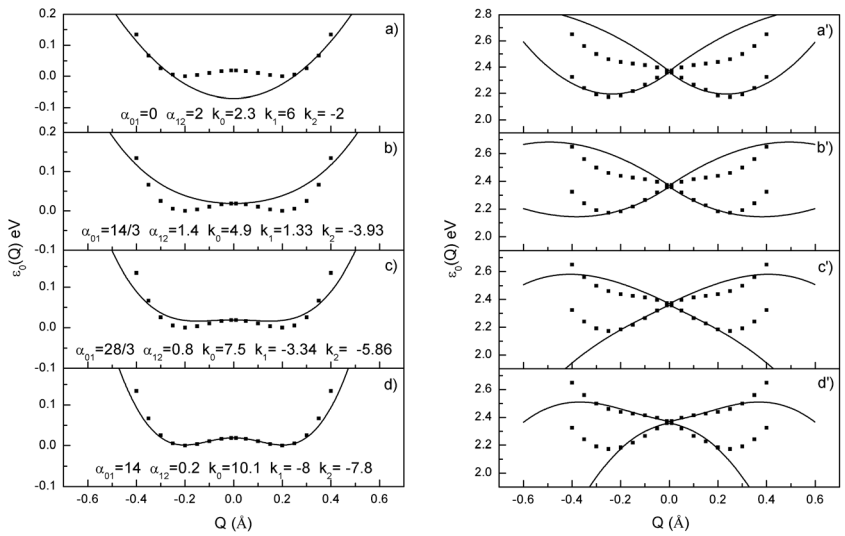


Fig. 3 APES of the $(1a_{1g} + 2a_{1g} + b_{1g}) \otimes B_{1g}$ problem *vs.* the symmetrized coordinate $Q$ along the puckering mode $B_{1g}$. Square dots correspond to the APES using TDDFT and continuous line using the linear PJT model. (a–d) correspond to the ground state and (a′–d′) to the excited APES states.

 

stability for $Q = 0$. For the same parameters, in Fig. 3(a′) we observe that a coupling ($\alpha_{12} = 2.0$) between the excited states produces only a matching with the excited state $a_{1g}$ (lower branch). In Fig. 3(b–d and b′–d′) we show the change in the APES for the linear PJT model as we gradually increase $\alpha_{01}$ and decrease $\alpha_{12}$. Fig. 3(d) and (d′) show, for small $Q$ values, the case of the simultaneous matching for the unstable ground state with both excited states.

The above mentioned analysis shows that through the fitting to the TDDFT APES it is possible to estimate the PJT APES parameters in the linear coupling model, and therefore to explain the instability in the $D_{6h}$ high-symmetry point, $Q = 0$ (Fig. 3(d)). It is worth mentioning that the coupling between excited states has a good agreement with TDDFT only for $Q$ values lower than 0.2. In order to go beyond this value, it would be necessary to include the interactions with other excited states, coupled by other normal modes besides puckering. Hence, the puckering effect is dominant for $Q$ values near the high-symmetry point, coinciding with our predicted distortion direction.

### 3.2 Properties of the $D_{3d}$ $Au_7^+$ cluster

In this section we present the structural, electronic and vibrational properties of the $D_{3d}$ $Au_7^+$ cluster that results from the PJT symmetry breaking. In Table 3 we present the HOMO–LUMO energy gap ($\Delta E_{HL}$), distances between gold atoms ($d_{Au-Au}$) and dihedral angle calculations for twelve different functional/basis combinations and compared with results reported in the literature. As can be seen from this Table, all methods predict a 3D structure with a dihedral angle varying from 23.2° to 36.1°. The ranges of center-vertex ($d_{cv}$) and vertex–vertex ($d_{vv}$) distances obtained in this work using the LANL2DZ and Stuttgart pseudopotentials are between 2.741 and 2.778 and 2.767 and 2.808 respectively. These ranges are in agreement with those reported in the literature.[27,40] Our ZORA calculations predict bond lengths in the range from 2.680 to 2.726 Å, with a range lower than the non-ZORA calculations; this behavior is consistent with that predicted for $Au_7^+$ in $D_{6h}$ symmetry (see Table 1). The most relevant effect of including the spin-orbit term can be seen in the narrowing of the HOMO–LUMO gap. This is due to the additional splitting of the electronic states, predicting values between 0.42 and 0.64 eV smaller than the other methods, with the exception of B3LYP, which overestimates this gap for 1.14 eV respect PBE(SR ZORA). As in the $D_{6h}$ case, the HL gaps obtained for this cluster are larger than those reported for $C_{60}$ (1.57 eV)[64] and $Au_{20}$ with symmetry $T_d$.[62] The dispersion correction effect in this case is also negligible.

Table 3 Electronic and structural properties for the $D_{3d}$ $Au_7^+$ cluster for different methods[a]

| Functional/basis | $\Delta E_{HL}$ | $d_{Au-Au}$ | Dihedral angle |
|---|---|---|---|
| B3LYP/LANL2DZ | 2.97 | 2.778, 2.808 | 32.6 |
| B3LYP/STUTTGART | 2.97 | 2.778, 2.799 | 27.4 |
| BP86/LANL2DZ | 1.91 | 2.743, 2.778 | 35.2 |
| BP86/STUTTGART | 1.88 | 2.747, 2.767 | 27.0 |
| PBE/LANL2DZ | 1.91 | 2.741, 2.778 | 36.1 |
| PBE/STUTTGART | 1.88 | 2.747, 2.767 | 26.7 |
| M06L (SR ZORA)/QZ4P | 2.05 | 2.711, 2.726 | 23.2 |
| TPSS (SR ZORA)/QZ4P | 1.92 | 2.681, 2.699 | 25.8 |
| TPSS-D (SR ZORA)/QZ4P | 1.95 | 2.673, 2.707 | 35.4 |
| PBE(SR ZORA)/QZ4P | 1.83 | 2.696, 2.715 | 26.5 |
| PBE-D (SR ZORA)/QZ4P | 1.85 | 2.690, 2.717 | 31.3 |
| PBE(SO ZORA)/QZ4P | 1.41 | 2.680, 2.704 | 29.8 |
| B3LYP/LANL2DZ[40] | | 2.779, 2.807 | 31.6 |
| B3LYP/ERMLER[40] | | 2.747, 2.773 | 31.5 |
| BP86/LANL2DZ[40] | | 2.750, 2.777 | 27.5 |

[a] HOMO–LUMO energy gap $\Delta E_{HL}$ (eV), distances Au–Au ($d_{Au-Au}$, Å) and dihedral angle (°). On the third column the values correspond to center-vertex and the vertex–vertex distances respectively.

The cluster $Au_7^+$ with symmetry $D_{3d}$, like $D_{6h}$, possesses 15 modes of vibration with 10 different frequencies, whose representation is given by the decomposition

$$\Gamma_{vib} = 2A_{1g} + 2E_g + A_{1u} + 2A_{2u} + 3E_u \quad (7)$$

and their frequencies are shown in Table 4. From these, four normal modes are Raman active ($2A_{1g} + 2E_g$), five are IR active ($2A_{2u} + 2E_u$) and only one is optically silent ($A_{1u}$), having therefore one more Raman and two more IR than the corresponding with $D_{6h}$ symmetry. The $2A_{1g}$ mode corresponds to the breathing mode, and the $1A_{1g}$ mode is predicted, from the STUTTGART and SR ZORA functional, with the lowest frequency; whereas for the LANL2DZ and SO ZORA is the second lowest. This mode corresponds to the puckering mode in $D_{6h}$ which has an imaginary frequency. The highest frequency corresponds to an IR-active mode ($3E_u$) with very low intensity (0.001 and 0.01 km mol$^{-1}$ for SR ZORA and SO ZORA respectively). The $1A_{2u}$ and $2E_u$ IR-active modes present the highest intensity.

### 3.3 Spectral properties

In order to show the effect of puckering on the $Au_7^+$ cluster, we present in Fig. 4a and b, the calculated SR ZORA Raman and IR

Table 4 Active normal mode frequencies for the $D_{3d}$ $Au_7^+$ cluster[a]

| Method | $\omega_{1A_{1g}}$ | $\omega_{2A_{1g}}$ | $\omega_{1E_g}$ | $\omega_{2E_g}$ | $\omega_{1A_{2u}}$ | $\omega_{2A_{2u}}$ | $\omega_{1E_u}$ | $\omega_{2E_u}$ | $\omega_{3E_u}$ |
|---|---|---|---|---|---|---|---|---|---|
| B3LYP/LANL2DZ | 15.7 | 111.7 | 59.1 | 104.6 | 36.3 | 62.6 | 13.8 | 71.5 | 155.4 |
| B3LYP/STUTTGART | 13.4 | 112.5 | 60.5 | 107.8 | 35.4 | 61.7 | 14.8 | 73.3 | 155.4 |
| PBE/LANL2DZ | 19.3 | 120.0 | 62.9 | 112.1 | 36.0 | 68.4 | 16.2 | 77.0 | 169.2 |
| PBE/STUTTGART | 3.6 | 117.6 | 59.7 | 109.8 | 31.4 | 58.9 | 10.1 | 71.0 | 161.1 |
| PBE(SR ZORA)/QZ4P | 17.1 | 124.3 | 66.8 | 122.0 | 35.1 | 67.2 | 18.0 | 84.1 | 174.1 |
| PBE(SO ZORA)/QZ4P | 21.3 | 127.6 | 69.1 | 123.8 | 31.6 | 71.0 | 19.1 | 85.5 | 179.5 |

[a] Raman-active ($\omega_{1A_{1g}}$, $\omega_{2A_{1g}}$, $\omega_{1E_g}$ y $\omega_{2E_g}$) and IR-active ($\omega_{1A_{2u}}$, $\omega_{2A_{2u}}$, $\omega_{1E_u}$, $\omega_{2E_u}$ and $\omega_{3E_u}$) normal modes frequencies in cm$^{-1}$.

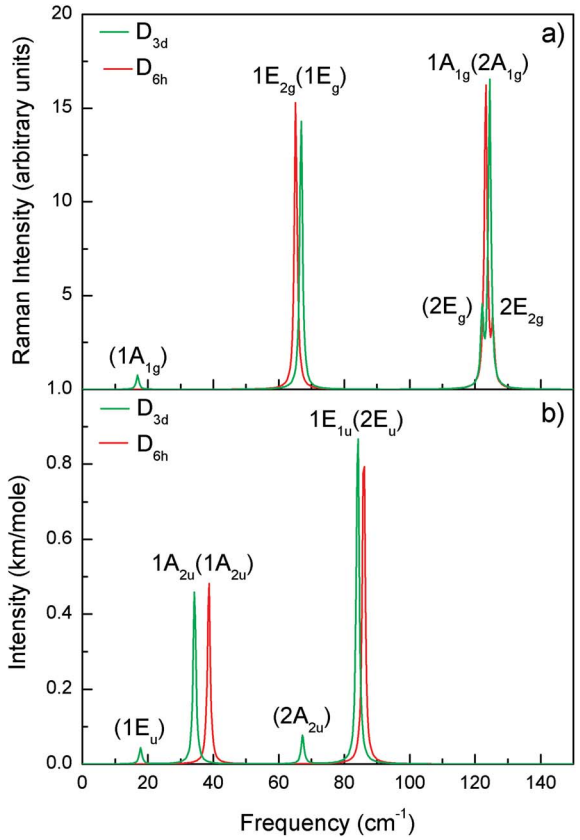


Fig. 4 Vibrational spectra for $Au_7^+$ cluster in symmetries $D_{3d}$ and $D_{6h}$. Intensities (a) Raman and (b) IR. The label on top of each peak corresponds to the normal mode irreps: irrep($D_{6h}$)(irrep($D_{3d}$)).

spectra in both $D_{3d}$ and $D_{6h}$ symmetries. For the $D_{6h}$ symmetry, the Raman spectrum shows all the three active modes mentioned in Section 3.1 and only two IR (the $3E_u$ has a higher frequency and very low intensity). These modes remain active after puckering, however the $1E_{2g}$ and $1A_{1g}$ Raman modes suffer a blueshift of 1.64 and 1.00 $cm^{-1}$ respectively, while the $2E_{2g}$ mode shows a redshift of 3.31 $cm^{-1}$. The IR spectrum only presents redshift (3.90 $cm^{-1}$ for the $1A_{2u}$ mode and 1.83 $cm^{-1}$ for the $1E_{1u}$ mode). There is one new Raman active mode ($1A_{1g}$) coming from the puckering mode $B_{1g}$ and two new IR modes

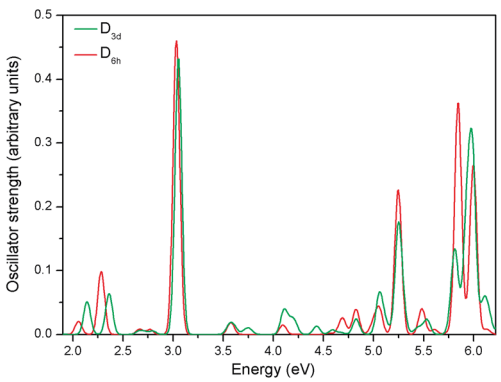


Fig. 5 UV-vis spectra of the $Au_7^+$ cluster in symmetries $D_{3d}$ and $D_{6h}$.

($1E_u$ and $2A_{2u}$ with intensities 0.04 and 0.08 km $mol^{-1}$ respectively) from the $E_{2u}$ and $B_{2u}$ $D_{6h}$ original modes. It is worth mentioning that the SO ZORA spectra present similar qualitative behavior, although with larger shifts. Their corresponding Raman values show blueshifts of 2.00 and 1.5 $cm^{-1}$, and redshift of 4.3 $cm^{-1}$; while the IR redshifts are 5.5 and 2.4 $cm^{-1}$.

Changes due to puckering in the calculated UV-vis spectrum are shown in Fig. 5, which is naturally divided into two zones: visible (2–3 eV) and UV (3.5 eV and beyond). The visible zone is reminiscent to that obtained by S. Lecoultre *et al.*[65] for $C_{2v}$-$Au_5$; this structure can be seen as a substructure of $Au_7^+$. The details of the visible spectra are included in Table 5, listing the optically allowed MO transitions with oscillator strengths $f > 0.1 \times 10^{-2}$. In Table 6 are tabulated the energy levels and irreps of the molecular orbitals participating in these transitions. The visible zone consists of five excitations for the $D_{6h}$ symmetry ($4e_{1u}$ and $1a_{2u}$) and one more $a_{2u}$ for $D_{3d}$. Basically the excitations are between the same MO in both symmetries; however, there are differences on the relative weights for which each transitions contributes to the excitation. The blue shift (around 20 nm) for the first two peaks $1e_{1u}$ and $2e_{1u}$ due to puckering can be very well appreciated in Fig. 5. For the UV-zone, the changes are mainly on the heights of the peaks, although light shifts and new peaks around 4.2–4.5 eV might probably affect the luminescence properties of the cluster and could be used as a signature of puckering.

## 4 Conclusions

Through DFT and TDDFT joint calculations in the ZORA approximation, we have shown that the nondegenerate ground state of the $Au_7^+$ cluster in $D_{6h}$ symmetry presents an instability towards a puckering structure, similar to that found in some organic cyclic structures. It was shown that the puckering distortion results from a PJT electron–vibron coupling, which can be described in a first approximation, by a linear coupling of three electronic states (ground and two excited states) through the $B_{1g}$ puckering vibrational mode. Our linear model is able to predict simultaneously the APES behavior for the ground and the two excited states. This is valid only for values of the symmetrized coordinate of 0.2 around the maximum symmetry point; beyond that range, it would be necessary to use either a nonlinear model or to take into account another vibronic interactions between excited states besides the puckering mediated mode. The calculated vibrational spectra for both symmetries show strong similarities, however the corresponding to the $D_{3d}$ symmetry has particular features that are indicative of the puckering modes. In particular, when compared to the $D_{6h}$ spectrum, we would like to highlight the red shift of the $2E_{2g}$ Raman mode of 3.31 $cm^{-1}$ and the $1A_{2u}$ IR of 3.90 $cm^{-1}$ (4.3 and 5.5 $cm^{-1}$ for SO ZORA), and the new Raman ($1A_{1g}$) and two IR ($1E_u$ and $2A_{2u}$) modes. The UV-vis spectra also show some differences. For the first two $e_{1u}$ transitions a blue shift of around 20 nm is predicted, and new transitions appear in the energy range of 4.2–4.5 eV, which can produce different luminescence properties. These features might be used to experimentally distinguish between the two

 

Table 5 Calculated excitation energies for the $D_{6h}$ and $D_{3d}$ $Au_7^+$ clusters[a]

| $D_{6h}$ | | | | | | $D_{3d}$ | | | |
|---|---|---|---|---|---|---|---|---|---|
| | $E$ | $f$ | MO transition | $w$ | | $E$ | $f$ | MO transition | $w$ |
| $1e_{1u}$ | 2.06 | 2.06 | $18b_{2u} \rightarrow 30e_{2g}$ | 0.52 | $1e_u$ | 2.14 | 5.12 | $46e_u \rightarrow 46e_g$ | 0.64 |
| | | | $32e_{1u} \rightarrow 30e_{2g}$ | 0.45 | | | | $32a_{2u} \rightarrow 46e_g$ | 0.27 |
| $2e_{1u}$ | 2.28 | 9.86 | $18b_{2u} \rightarrow 30e_{2g}$ | 0.42 | $3e_u$ | 2.36 | 6.36 | $2a_{2u} \rightarrow 46e_g$ | 0.60 |
| | | | $32e_{1u} \rightarrow 30e_{2g}$ | 0.40 | | | | $46e_u \rightarrow 46e_g$ | 0.21 |
| $3e_{1u}$ | 2.67 | 0.84 | $31e_{1u} \rightarrow 30e_{2g}$ | 0.64 | $4e_u$ | 2.66 | 0.48 | $45e_u \rightarrow 46e_g$ | 0.91 |
| | | | $32e_{1u} \rightarrow 27a_{1g}$ | 0.18 | | | | | |
| | | | $17b_{2u} \rightarrow 30e_{2g}$ | 0.15 | | | | | |
| | | | | | $2a_{2u}$ | 2.71 | 0.32 | $45e_u \rightarrow 46e_g$ | 0.96 |
| $1a_{2u}$ | 2.77 | 0.77 | $14e_{2u} \rightarrow 30e_{2g}$ | 0.99 | $3a_{2u}$ | 2.80 | 0.45 | $44e_u \rightarrow 46e_g$ | 0.96 |
| $5e_{1u}$ | 3.03 | 46.0 | $32e_{1u} \rightarrow 27a_{1g}$ | 0.66 | $7e_u$ | 3.05 | 43.5 | $46e_u \rightarrow 36a_{1g}$ | 0.61 |
| | | | $17b_{2u} \rightarrow 30e_{2g}$ | 0.11 | | | | $31a_{2u} \rightarrow 46e_g$ | 0.12 |

[a] Energy $E$ (eV), oscillator strengths ($f \times 10^{-2}$), corresponding dominant occupied to virtual MO transitions and weight ($w$) of the first optically allowed excited states.

Table 6 Orbital energies (in eV) of the ground state for the $D_{6h}$ and $D_{3d}$ $Au_7^+$ clusters

| | $D_{6h}$ | | $D_{3d}$ | |
|---|---|---|---|---|
| MO | irrep | $E$ | irrep | $E$ |
| HOMO-12 | $17b_{2u}$ | −11.055 | $42e_g$ | −11.185 |
| HOMO-11 | $14e_{2u}$ | −11.045 | $31a_{2u}$ | −11.057 |
| HOMO-10 | $31e_{1u}$ | −11.034 | $44e_u$ | −11.043 |
| HOMO-9 | $15e_{1g}$ | −11.032 | $34a_{1g}$ | −11.021 |
| HOMO-8 | $26a_{1g}$ | −11.032 | $45e_u$ | −10.973 |
| HOMO-7 | $9\ b_{1g}$ | −10.970 | $35a_{1g}$ | −10.954 |
| HOMO-6 | $28e_{2g}$ | −10.887 | $43e_g$ | −10.835 |
| HOMO-5 | $16e_{1g}$ | −10.720 | $44e_g$ | −10.680 |
| HOMO-4 | $18b_{2u}$ | −10.514 | $32a_{2u}$ | −10.605 |
| HOMO-3 | $4ae_{1u}$ | −10.438 | $14a_{1u}$ | −10.564 |
| HOMO-2 | $29e_{2g}$ | −10.401 | $13a_{2g}$ | −10.327 |
| HOMO-1 | $9a_{2g}$ | −10.310 | $45e_g$ | −10.299 |
| HOMO | $32e_{1u}$ | −10.225 | $46e_u$ | −10.212 |
| LUMO | $30e_{2g}$ | −8.430 | $46e_g$ | −8.380 |
| LUMO+1 | $27a_{1g}$ | −7.497 | $36a_{1g}$ | −7.462 |

structures. Our prediction of a structural instability of the 2D $D_{6h}$ symmetry for the nondegenerate ground state of the $Au_7^+$ cluster, ending in a 3D puckered $D_{3d}$ structure, is consistent with reported theoretical structures by Gloess *et al.*, and Remacle and Kryachko; and also with the ion mobility data by Gilb *et al.*, since in average, it has approximately the same cross section that the planar hexagonal structure, having therefore the same mobility properties, hence being the two structures indistinguishable by this particular experimental technique.

## Acknowledgements

We are thankful with the computer facilities of the Dirección General de Cómputo y de Tecnologías de la Información (DGTIC-UNAM) and with the GENERAL COORDINATION OF INFORMATION AND COMMUNICATIONS TECHNOLOGIES (CGSTIC) at CINVESTAV for providing HPC resources on the Hybrid Cluster Supercomputer "Xiuhcoatl". B. Molina acknowledges support by PAPIIT-DGAPA, UNAM IN119811.

## References

1 M. Haruta, *Catal. Today*, 1997, **36**, 153–166.
2 B. Yoon, H. Häkkinen, U. Landman, A. S. Wörz, J.-M. Antonietti, S. Abbet, K. Judai and U. Heiz, *Science*, 2005, **307**, 403–407.
3 B. S. de Bas, M. J. Ford and M. B. Cortie, *J. Mol. Struct.: THEOCHEM*, 2004, **686**, 193–205.
4 M. P. Johansson, A. Lechtken, D. Schooss, M. M. Kappes and F. Furche, *Phys. Rev. A*, 2008, **77**, 053202.
5 P. Pyykkö, *Angew. Chem., Int. Ed.*, 2004, **43**, 4412–4456.
6 P. Schwerdtfeger and M. Lenin, *Gold Chemistry Applications and Future directions in the Life Sciences*, Wiley-VCH, Weinheim, Germany, 1st edn, 2009.
7 P. Pyykkö, *Annu. Rev. Phys. Chem.*, 2012, **63**, 45–64.
8 P. Pyykkö and N. Runeberg, *Angew. Chem., Int. Ed.*, 2002, **41**, 2174–2176.
9 A. J. Karttunen, M. Linnolahti, T. A. Pakkanen and P. Pyykkö, *Chem. Commun.*, 2008, 465–467.
10 S. Bulusu and X. C. Zeng, *J. Chem. Phys.*, 2006, **125**, 154303.
11 F. Furche, R. Ahlrichs, P. Weis, C. Jacob, S. Gilb, T. Bierweiler and M. M. Kappes, *J. Chem. Phys.*, 2002, **117**, 6982–6990.
12 H. Häkkinen, M. Moseler and U. Landman, *Phys. Rev. Lett.*, 2002, **89**, 033401.
13 W. Fa, C. Luo and J. Dong, *Phys. Rev. B: Condens. Matter Mater. Phys.*, 2005, **72**, 205428.
14 X.-G. Xiong, W.-H. Xu, J. Li and P. Pyykkö, *Int. J. Mass Spectrom.*, 2013, **354–355**, 15–18.
15 E. M. Fernández, J. M. Soler and L. C. Balbás, *Phys. Rev. B: Condens. Matter Mater. Phys.*, 2006, **73**, 235433.
16 B. Assadollahzadeh and P. Schwerdtfeger, *J. Chem. Phys.*, 2009, **131**, 064306.
17 D. A. Götz, R. Schäfer and P. Schwerdtfeger, *J. Comput. Chem.*, 2013, **34**, 1975–1981.
18 M. Zhang, S.-B. Yang, X.-J. Feng, L.-X. Zhao, H.-Y. Zhang and Y.-H. Luo, *Eur. Phys. J. D*, 2013, **67**, 11.

19 P. Weis, *Int. J. Mass Spectrom.*, 2005, **245**, 1–13.
20 E. M. Fernández, J. M. Soler, I. L. Garzón and L. C. Balbás, *Phys. Rev. B: Condens. Matter Mater. Phys.*, 2004, **70**, 165403.
21 A. V. Walker, *J. Chem. Phys.*, 2005, **122**, 094310.
22 P. Gruene, D. M. Rayner, B. Redlich, A. F. G. van der Meer, J. T. Lyon, G. Meijer and A. Fielicke, *Science*, 2008, **321**, 674–676.
23 Z. Y. Li, N. P. Young, M. M. Di Vece, S. Palomba, A. L. Bleloch, B. C. Curley, R. L. Johnston, J. Jiang and J. Yuan, *Nature*, 2008, **451**, 46–49.
24 S. M. Lang and T. M. Bernhardt, *Phys. Chem. Chem. Phys.*, 2012, **14**, 9255–9269.
25 S. Bulusu, X. Li, L.-S. Wang and X. C. Zeng, *Proc. Natl. Acad. Sci. U. S. A.*, 2006, **103**, 8326–8330.
26 X. Xing, B. Yoon, U. Landman and J. H. Parks, *Phys. Rev. B: Condens. Matter Mater. Phys.*, 2006, **74**, 165423.
27 A. N. Gloess, H. Schneider, J. M. Weber and M. M. Kappes, *J. Chem. Phys.*, 2008, **128**, 114312.
28 H. Häkkinen and U. Landman, *Phys. Rev. B: Condens. Matter Mater. Phys.*, 2000, **62**, R2287–R2290.
29 W. Fa and J. Dong, *Appl. Phys. Lett.*, 2006, **89**, 013117.
30 J. C. Idrobo, W. Walkosz, S. F. Yip, S. Öğüt, J. Wang and J. Jellinek, *Phys. Rev. B: Condens. Matter Mater. Phys.*, 2007, **76**, 205422.
31 A. Deka and R. C. Deka, *J. Mol. Struct.: THEOCHEM*, 2008, **870**, 83–93.
32 M. Mantina, R. Valero and D. G. Truhlar, *J. Chem. Phys.*, 2009, **131**, 064706.
33 L. Ferrighi, B. Hammer and G. K. H. Madsen, *J. Am. Chem. Soc.*, 2009, **131**, 10605–10609.
34 Y.-K. Shi, Z. H. Li and K.-N. Fan, *J. Phys. Chem. A*, 2010, **114**, 10297–10308.
35 L. M. Wang and L. S. Wang, *Nanoscale*, 2012, **5**, 4038–4053.
36 S. A. Serapian, M. J. Bearpark and F. Bresme, *Nanoscale*, 2013, **5**, 6445–6457.
37 L. A. Mancera and D. M. Benoit, *Phys. Chem. Chem. Phys.*, 2013, **15**, 1929–1943.
38 E. Fabiano, L. A. Constantin and F. Della Sala, *J. Chem. Phys.*, 2011, **134**, 194112.
39 S. Gilb, P. Weis, F. Furche, R. Ahlrichs and M. M. Kappes, *J. Chem. Phys.*, 2002, **116**, 4094–4101.
40 F. Remacle and E. S. Kryachko, *J. Chem. Phys.*, 2005, **122**, 044304.
41 A. D. Becke, *J. Chem. Phys.*, 1993, **98**, 5648–5652.
42 J. P. Perdew, K. Burke and M. Ernzerhof, *Phys. Rev. Lett.*, 1996, **77**, 3865–3868.
43 D. Andrae, U. Häußermann, M. Dolg, H. Stoll and H. Preuß, *Theor. Chim. Acta*, 1990, **77**, 123–141.
44 A. P. Sergeeva and A. I. Boldyrev, *J. Clust. Sci.*, 2011, **22**, 321–329.
45 P. J. Hay and W. R. Wadt, *J. Chem. Phys.*, 1985, **82**, 270–283, 299–310, 284–298.
46 R. B. Ross, J. M. Powers, T. Atashroo, W. C. Ermler, L. A. LaJohn and P. A. Christiansen, *J. Chem. Phys.*, 1990, **93**, 6654–6670.
47 A. D. Becke, *Phys. Rev. A*, 1988, **38**, 3098–3100.
48 J. P. Perdew, *Phys. Rev. B: Condens. Matter Mater. Phys.*, 1986, **33**, 8822–8824.
49 I. Y. Ogurtsov, G. Munteanu, L. Bantush and I. B. Bersuker, *J. Mol. Struct.: THEOCHEM*, 2001, **541**, 141–148.
50 T. Ichino, S. W. Wren, K. M. Vogelhuber, A. J. Gianola, W. C. Lineberger and J. F. Stanton, *J. Chem. Phys.*, 2008, **129**, 084310.
51 Y. Liu, I. B. Bersuker, P. Garcia-Fernandez and J. E. Boggs, *J. Phys. Chem. A*, 2012, **116**, 7564–7570.
52 Y. Liu, I. B. Bersuker, W. Zou and J. E. Boggs, *J. Chem. Theory Comput.*, 2009, **5**, 2679–2686.
53 I. B. Bersuker, *Chem. Rev.*, 2013, **113**, 1351–1390.
54 I. B. Bersuker, *The Jahn-Teller Effect*, Cambridge University Press, Cambridge, 1st edn, 2006.
55 ADF, *Theoretical Chemistry*, SCM, Vrije Universiteit, Amsterdam, Netherlands, 2012, www.scm.com.
56 E. van Lenthe, E. J. Baerends and J. G. Snijders, *J. Chem. Phys.*, 1993, **99**, 4597–4610.
57 E. van Lenthe, A. van der Avoird and P. E. S. Wormer, *J. Chem. Phys.*, 1998, **108**, 4783–4796.
58 M. J. Frisch, *et al.*, *Gaussian03, C.01*, Gaussian Inc., Wallingford, CT, 2004.
59 J. Tao, J. P. Perdew, V. N. Staroverov and G. E. Scuseria, *Phys. Rev. Lett.*, 2003, **91**, 146401.
60 Y. Zhao and D. G. Truhlar, *Theor. Chem. Acc.*, 2008, **120**, 215–241.
61 B. Molina, J. R. Soto and J. J. Castro, *J. Phys. Chem. C*, 2012, **116**, 9290–9299.
62 J. Li, X. Li, H.-J. Zhai and L.-S. Wang, *Science*, 2003, **299**, 864–867.
63 B. Molina, J. R. Soto and A. Calles, *Rev. Mex. Fis.*, 2008, **54**, 314–318.
64 X. B. Wang, C.-F. Ding and L.-S. Wang, *J. Chem. Phys.*, 1999, **110**, 8217–8220.
65 S. Lecoultre, A. Rydlo, C. Félix, J. Buttet, S. Gilb and W. Harbich, *J. Chem. Phys.*, 2011, **134**, 074302.

 